A Model-Based Approach to Crack Sizing With Ultrasonic Arrays

Katherine M. M. Tant, Anthony J. Mulholland, and Anthony Gachagan

***Abstract*—Ultrasonic phased array systems have become increasingly popular in the last 10 years as tools for flaw detection and characterization within the nondestructive testing industry. The existence and location of flaws can often be deduced via images generated from the data captured by these arrays. A factor common to these imaging techniques is the subjective thresholding required to estimate the size of the flaw. This paper puts forward an objective approach which employs a mathematical model. By exploiting the relationship between the width of the central lobe of the scattering matrix and the crack size, an analytical expression for the crack length is reached via the Born approximation. Conclusions are then drawn on the minimum resolvable crack length of the method and it is thus shown that the formula holds for subwavelength defects. An analytical expression for the error that arises from the discrete nature of the array is then derived and it is observed that the method becomes less sensitive to the discretization of the array as the distance between the flaw and array increases. The methodology is then extended and tested on experimental data collected from welded austenitic plates containing a lack-of-fusion crack of 6 mm length. An objective sizing matrix (OSM) is produced by assessing the similarity between the scattering matrices arising from experimentally collected data with those arising from the Born approximation over a range of crack lengths and frequencies. Initially, the global minimum of the OSM is taken as the objective estimation of the crack size, giving a measurement of 7 mm. This is improved upon by the adoption of a multi-frequency averaging approach, with which an improved crack size estimation of 6.4 mm is obtained.**

I. Introduction

Many safety critical structures, such as those found in nuclear plants [1], oil pipelines [2], and in the aerospace industry [3], rely on key components that are constructed from heterogeneous materials. Ultrasonic nondestructive testing (NDT) uses high frequency mechanical waves to inspect these parts, ensuring they operate reliably without compromising their integrity. Within this field, considerable effort has been expended in exploiting the full matrix capture (FMC) [4], [5] collected by phased array inspections, in the hope of improving the methods currently used for the detection and characterization of defects. The current industry benchmark for interpreting the FMC is the total focusing method (TFM); a delay and sum imaging technique where the area of inspection is discretized into a grid and the sections of the signals from every transmit/receive pair relevant to each pixel are summed [4], [6]. However, inherent to the TFM [and other imaging algorithms [7]–[9]] is the need for an arbitrary dynamic threshold at which to size the defect. In this paper, a model-based crack sizing algorithm for zero-volume flaws is proposed so as to remove this subjectivity from crack size and orientation estimations. Work on objective crack sizing has previously been explored in [10], where both the maximum scattering amplitude and the half-width, half-maximum (HWHM) measurement of the pulse-echo response of a scattering matrix were shown to correlate with the crack length. The method presented here is similar only in its exploitation of the frequency domain scattering matrices that arise when an incident pressure wave is scattered by a flaw. Favoring the roots of the pulse-echo response plot over the HWHM, the proposed crack-sizing algorithm is immune to the effects of the transducer transfer function and is based on a mathematical formula rather than a numerically derived HWHM value.

To develop an understanding of the scattering of ultrasound waves [11, ch. 8] and to facilitate work on model based crack-sizing, an analytic mathematical model has been investigated. The Born approximation ([12], chapter 10; [13], chapter 6; [14], chapter 4) is a low-frequency, weak-scattering approximation for volumetric flaws. It estimates the scattering amplitude arising from an incident wave (traveling in a homogeneous host medium) of given direction coming into contact with a flaw. Despite its restrictions, it is very useful in relating the flaw response directly to the flaw geometry and can be used to simulate strong back-scattering from crack-like defects. For the purposes of this paper, the scattering of a pressure wave by an ellipsoidal inclusion in an elastic medium is considered. Restricting attention to the 2-D plane below the linear array (the crack is approximated as an ellipsoid with $a_3 = 0$, see Fig. 1), this is given by [12], equation 10.220:

$$A_n(\mathbf{e}_{\mathrm{i}}, \mathbf{e}_{\mathrm{s}}) = -\frac{a_1 a_2 B_{ln} f_l(\mathbf{e}_i, \mathbf{e}_s)}{|\mathbf{g}|^2 (r_{\mathrm{e}})^2} \times \left(\frac{\sin(k_{P0}|\mathbf{g}|r_{\mathrm{e}}) - k_{P0}|\mathbf{g}|r_{\mathrm{e}} \cos(k_{P0}|\mathbf{g}|r_{\mathrm{e}})}{k_{P0}|\mathbf{g}|r_{\mathrm{e}}} \right), \quad (1)$$

Manuscript received October 28, 2014; accepted March 14, 2015. This work was supported by the Engineering and Physical Sciences Research Council (grant number EP/I019731/1). This work was funded through the UK Research Centre in NDE Targeted Programme by the Engineering and Physical Sciences Research Council, National Nuclear Laboratory, Rolls Royce, Shell, Weidlinger, and Amec Foster Wheeler, who also provided the experimental sample.

K. M. M. Tant and A. J. Mulholland are with the Department of Mathematics and Statistics, University of Strathclyde, G1 1XH Glasgow, UK (e-mail: katy.tant@strath.ac.uk).

A. Gachagan is with the Centre for Ultrasonic Engineering, University of Strathclyde, G1 1XW Glasgow, UK.

DOI http://dx.doi.org/10.1109/TUFFC.2014.006809

This work is licensed under a Creative Commons Attribution 3.0 License.
For more information, see http://creativecommons.org/licenses/by/3.0/

where $\mathbf{e}_{\mathrm{i}}$ and $\mathbf{e}_{\mathrm{s}}$ are unit vectors in the transmission and reception directions, respectively; a_1 and a_2 represent the dimensions of the ellipsoidal flaw; k_{P0} is the wavenumber in the host material; $\mathbf{g} = \mathbf{e}_i - \mathbf{e}_s$; and r_{e} is the effective radius of the flaw, given by

$$r_{\mathrm{e}} = \sqrt{a_1^2(\mathbf{e}_q \cdot \mathbf{u}_1)^2 + a_2^2(\mathbf{e}_q \cdot \mathbf{u}_2)^2} \tag{2}$$

$$\text{with } \mathbf{e}_q = \frac{\mathbf{g}}{|\mathbf{g}|}. \tag{3}$$

Unit vectors $\mathbf{u}_1$ and $\mathbf{u}_2$ lie in the vertical plane along the major and minor axes of the flaw. The term $B_{ln}f_l(\mathbf{e}_i, \mathbf{e}_s)$ can be expressed as in [12, Eq. 10.218] and incorporates the material parameters of the host and flaw materials (here the subscripts refer to the nth component of the displacement vector due to the incident wave in the lth direction). By changing the range of angles that the transmission and reception directions ($\mathbf{e}_i$ and $\mathbf{e}_s$) can take, different array apertures can be simulated. The size, shape, and location of the defect and material properties can also be varied and hence allow comparison of the model to experimental data. For the method presented in this paper, the focus will be on crack-like flaws located under the center of the array. These will be simulated by setting the flaw dimensions so that $a_1 \gg a_2$, where $a = 2a_1$ is then taken to be the crack length and a_2 is close to zero. The flaw orientation refers to the angle θ that $\mathbf{u}_1$ makes with the x-axis.

By plotting the scattering amplitude as generated by the Born approximation for pairs of transmit/receive directions (chosen to mimic a linear array) a scattering matrix is produced. This matrix contains information on the location, size, form, and orientation of the defect [15]. By plotting these matrices, patterns can be observed and later exploited to objectively characterize flaws.

II. Model-Based Crack Sizing

Work has previously been carried out by Zhang *et al.* [10] on the extraction of key parameters (i.e., crack length and orientation) from scattering matrices for small crack-like defects. By empirical means, they showed that the half-width, half-maximum (HWHM) pulse-echo response plot of a scattering matrix decreased monotonically with crack length. One disadvantage of using the HWHM is that it is affected by the transducer response. Work on characterizing the field emitted and received by the transducer is discussed in [16], [17], and the scattered wave from the flaw can, in principle, be recovered by deconvolving the function describing the transducer effects from the received signal. This increases the consonance of the HWHM in relation to the scattering profile of the flaw. However, this complication can be removed by concentrating on the zeros of the pulse-echo response as these are independent of the transducer effects. The crack-sizing algorithm as developed and discussed in this paper is based on this idea, and in contrast to the work in [10], does not rely on an empirically attained correlation but instead is derived analytically.

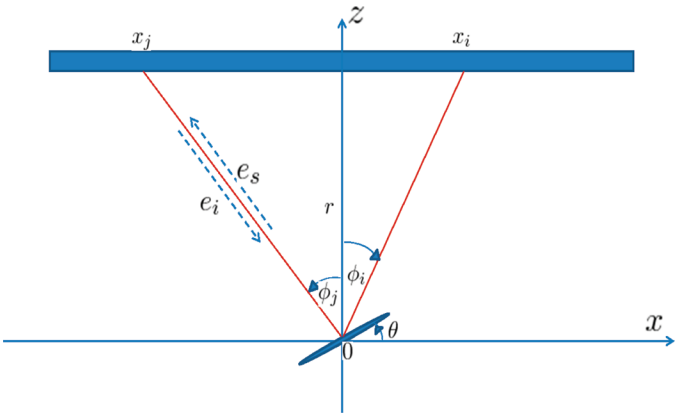

Fig. 1. Diagram depicting the general situation where the crack is oriented at an angle θ relative to the x-axis. x_i and x_j are the element locations corresponding to the innermost zero of the pulse-echo response and ϕ_i and ϕ_j are the corresponding angles.

A. The Zero-Degree Crack Case

The diagonal elements of a scattering matrix relate to the case where $\mathbf{e}_{\mathrm{s}} = -\mathbf{e}_i$, also known as the pulse-echo response. As the ratio of crack length to wavelength increases, it is observed that the central lobe of the scattering matrix narrows (see Fig. 2). This narrowing can be measured by the distance between the zeros that lie either side of the global maximum of the pulse-echo response of the scattering matrix. Note that when using this method with discrete array elements, these zeros are replaced by the locations of the local minima in the pulse-echo response, which relate to the ith and jth array element with position x_i and x_j. The ith transmitted wave unit vector is

$$\mathbf{e}_{\mathrm{i}} = -\frac{(x_i, r)}{|(x_i, r)|}, \tag{4}$$

where r is the distance of the flaw from the array. To derive a formula for the length of the crack, it is temporarily assumed that x_i is a continuous variable x, where $x = 0$ corresponds to the center of the ultrasonic array. From (1), it follows that the zero in the pulse-echo response satisfies

$$\sin(k_{P0}|\mathbf{g}|r_{\mathrm{e}}) - k_{P0}|\mathbf{g}|r_{\mathrm{e}}\cos(k_{P0}|\mathbf{g}|r_{\mathrm{e}}) = 0. \tag{5}$$

From (2) and (5) it can be written that

$$M = 2k_{P0}\sqrt{a_1^2(\mathbf{e}_q \cdot \mathbf{u}_1)^2 + a_2^2(\mathbf{e}_q \cdot \mathbf{u}_2)^2}, \tag{6}$$

where $M = 4.49341$ (the first root of $\tan M = M$), and for the pulse-echo case, $\mathbf{e}_q = \mathbf{e}_i$. Let us begin by examining the case where the crack is oriented at 0° (parallel to the array). Because $\mathbf{u}_1$ and $\mathbf{u}_2$ are equal to $[1,0]^T$ and $[0,1]^T$, respectively, by substituting $k_{P0} = 2\pi/\lambda$ and rearranging

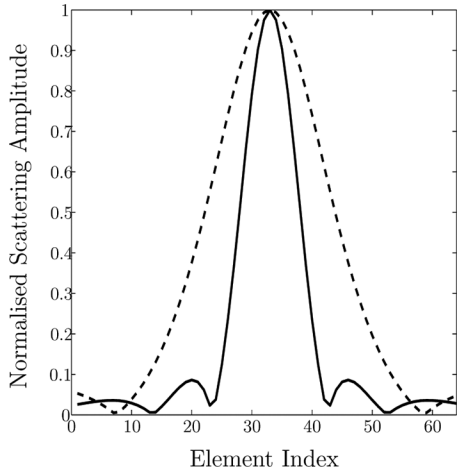

Fig. 2. Pulse-echo responses as generated by the Born approximation for cracks embedded in a homogeneous medium, lying 50 mm below and parallel to a linear array of 64 elements with a/λ values of 1 (dashed line) and 2 (full line).

(6), an explicit expression for the crack length a can be obtained,

$$a = 2a_1 = \frac{2}{x_i}\left(\frac{M^2\lambda^2}{16\pi^2}(x_i^2 + r^2) - a_2^2 r^2\right)^{1/2}. \quad (7)$$

An expression for x_i can also be derived in this manner,

$$x_i = r\sqrt{\frac{(M/2\pi)^2 - (2a_2/\lambda)^2}{(2a_1/\lambda)^2 - (M/2\pi)^2}}. \quad (8)$$

For this case, the central lobe in the pulse-echo response is positioned centrally about $x = 0$ (the center of the ultrasonic array). Due to the symmetry about $x = 0$, the first positive root x_i is related to the first negative root x_j via $x_i = -x_j$. The width of the main lobe is therefore $2x_i$. Eq. (8) suggests that as the depth of the flaw, r, increases, the width of the main lobe in the scattering matrix increases. On reflection, it can be understood that as the depth increases, the angle between the outermost array elements decreases and hence the array captures less of the scattering profile, resulting in a scattering matrix with a wider central lobe. As interest is restricted to crack-like flaws (where $a_1 \gg a_2$), (8) gives rise to the following conditions on a_1 and a_2:

$$\frac{2a_1}{\lambda} > \frac{M}{2\pi} > \frac{2a_2}{\lambda}. \quad (9)$$

This condition shows (7) will only hold for cracks where $a/\lambda > M/2\pi = 0.71529$. This lower bound lies within the interval $0.1 \leq 2\pi a/\lambda \leq 10$ in which it has been shown previously in [18] that use of the Born approximation is valid. Another consideration to be taken into account is the length of the array aperture. To have roots on the pulse-echo diagonal, x_i must fall within the limits of the aperture. Let L be the length of the linear array, and let the flaw be located beneath its center. From (8), as the crack size decreases, then x_i increases. So, the smallest crack size that can be resolved for a given aperture coincides with $x_i = L/2$. Hence, (8) gives

$$\frac{L}{2} = r\sqrt{\frac{(M/2\pi)^2 - (2a_2/\lambda)^2}{(a_{\min}/\lambda)^2 - (M/2\pi)^2}}. \quad (10)$$

That is,

$$\hat{a}_{\min} = \frac{a_{\min}}{\lambda} = \sqrt{(M/2\pi)^2 + \frac{(M/2\pi)^2 - (2a_2/\lambda)^2}{(L/2r)^2}}. \quad (11)$$

Allowing $a_2 = 0$, to approximate a crack, the minimum resolvable crack length is given by

$$\hat{a}_{\min} = \sqrt{(M/2\pi)^2 + (Mr/\pi L)^2}. \quad (12)$$

Once again, it can be observed that as $L \to \infty$, then $\hat{a}_{\min} \to M/2\pi = 0.71529$, giving the smallest crack size that can be resolved relative to the wavelength. Conversely, as the distance of the flaw from the array increases, so that $r/L \gg 1/2$, then the smallest crack size that can be resolved increases, $\hat{a}_{\min} \to Mr/\pi L$, since the width of the main lobe in the scattering matrix widens. It should be borne in mind, however, that there is no wave attenuation in the mathematical model and this method is based on the scattering wave coefficient rather than the scattering wave amplitude received by the array.

B. The Effect of Crack Orientation on Crack Sizing

In this section, the crack is now oriented so that the array and the vector $\mathbf{u}_1$ are no longer parallel. Let the crack now be rotated by an angle θ in the anti-clockwise direction. Hence, $\mathbf{u}_1 = (\cos\theta, \sin\theta)$ and $\mathbf{u}_2 = (-\sin\theta, \cos\theta)$. The analysis is still focused on the pulse-echo response values, so it still holds that $\mathbf{e}_q = \mathbf{e}_i$, with $\mathbf{e}_i$ as set in (4). Relating the values of x_i and r to the angle ϕ_i as in Fig. 1, then $(\mathbf{e}_q \cdot \mathbf{u}_1) = -\sin(\phi_i + \theta)$, and similarly, $(\mathbf{e}_q \cdot \mathbf{u}_2) = -\cos(\phi_i + \theta)$. It follows then, from (6), that

$$M = \frac{4\pi}{\lambda}\sqrt{a_1^2 \sin^2(\phi_i + \theta) + a_2^2 \cos^2(\phi_i + \theta)}, \quad (13)$$

which results in an expression for the crack length

$$a = \sqrt{\frac{M^2\lambda^2}{4\pi^2}\csc^2(\phi_i + \theta) - 4a_2^2 \cot^2(\phi_i + \theta)}. \quad (14)$$

However, there are now two unknowns, a and θ. The introduction of the crack orientation angle θ calls for the use of the two innermost roots, as these describe the width and location of the main lobe of the scattering matrix. These relate to element positions x_i and x_j, which translate to the angles ϕ_i and ϕ_j as in shown Fig. 1. Eq. (14) can then be used to give

$$\frac{M^2\lambda^2}{16\pi^2}\csc^2(\phi_i+\theta)-a_2^2\cot^2(\phi_i+\theta) = \frac{M^2\lambda^2}{16\pi^2}\csc^2(\phi_j+\theta)-a_2^2\cot^2(\phi_j+\theta), \tag{15}$$

which can be solved for θ. Note that it is possible to rewrite (13) in terms of element location x_i as opposed to the angle ϕ_i,

$$M^2 = \frac{16\pi^2 a_1^2}{\lambda^2}\left(\frac{x_i\cos\theta}{\sqrt{x_i^2+r^2}}+\frac{r\sin\theta}{\sqrt{x_i^2+r^2}}\right)^2 + \frac{16\pi^2 a_2^2}{\lambda^2}\left(\frac{r\cos\theta}{\sqrt{x_i^2+r^2}}-\frac{x_i\sin\theta}{\sqrt{x_i^2+r^2}}\right)^2. \tag{16}$$

Rearranging for a gives

$$a = \frac{2\sqrt{(M^2\lambda^2/16\pi^2)(x_i^2+r^2)-a_2^2(r\cos\theta-x_i\sin\theta)^2}}{(x_i\cos\theta+r\sin\theta)}. \tag{17}$$

Expressing a in this manner allows for exploration of the limitations of the algorithm due to the discretization of the array by the array pitch (see Section II-C). Observe that by substituting in $\theta = 0$, re-creating the 0° oriented crack case, (7) is recovered.

Having calculated the crack orientation using (15), it is now possible to substitute this value into (14) and retrieve the crack length. Once again, conclusions can be drawn on the minimum aperture required for the algorithm to succeed. As the crack rotates from 0° to 90°, anti-clockwise, it is apparent that the array must be extended to the left to capture the two zeros along the pulse-echo response. Referring to Fig. 1, the locations of the first and last elements of the shortest suitable array can be calculated as $x_i = r\tan(\phi_i)$. Exact values for ϕ_i and ϕ_j can be calculated via (14):

$$\phi_i = \sin^{-1}\left(\sqrt{\frac{M^2\lambda^2-16\pi^2a_2^2}{16\pi^2(a_1^2-a_2^2)}}\right)-\theta, \tag{18}$$

$$\phi_j = -\sin^{-1}\left(\sqrt{\frac{M^2\lambda^2-16\pi^2a_2^2}{16\pi^2(a_1^2-a_2^2)}}\right)-\theta. \tag{19}$$

The minimum aperture length required is then given by

$$L = r\left|\tan(\phi_i)-\tan(\phi_j)\right|. \tag{20}$$

C. Errors Arising From Discretization of the Array

The implementation of this crack-sizing algorithm is dependent on the estimation of experimental parameters such as the array element pitch and the wavelength. It is of particular interest to analyze the maximum errors that can occur due to the discretization of x arising from the array design. Because the ultrasonic array is composed of a discrete set of elements, positioned at regular intervals called the pitch p, then the estimation of x_i that is extracted from the scattering matrix will only be approximate. The value of the crack size that is then predicted using this approximate value of x_i is denoted by a^{D}. The error due to this discretization (ε^{D}) is then given by the difference between the known a and a^{D}. The formulae for the crack length can be analyzed, and an expression for the maximum error ε^{M} due to discretization by the array pitch can be subsequently derived. The resulting expression for the error can be further approximated to provide an analytical form that shows its dependency on the model parameters. This error is then denoted ε^{A}. In the worst case scenario, the estimated value for x_i can potentially be out by up to one pitch. This is demonstrated in Fig. 3 where it can be seen that the minimum of the discretized pulse-echo response, which occurs at x_i, is further from the actual root (marked by the hollow disc) than array element x_{i-1}.

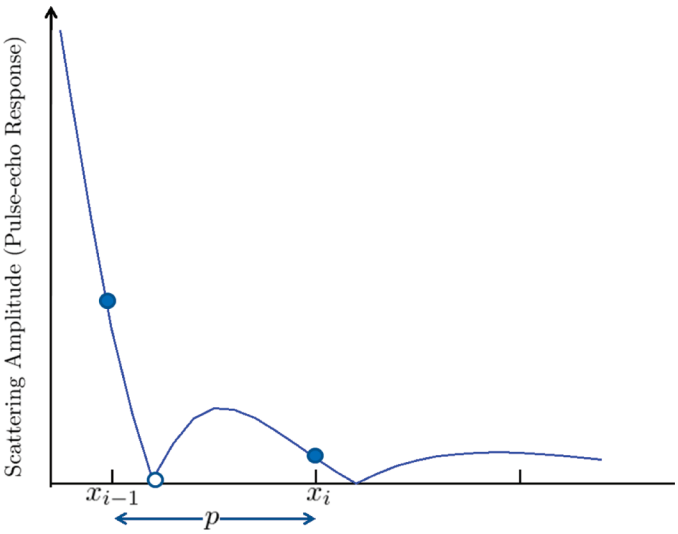

Fig. 3. A segment of the pulse-echo response. Due to discretization by the array pitch, the minimum must be chosen from a set of discrete points (shaded discs). However, the minimum does not always correspond with the element lying closest to the location of the actual root as predicted by the model (hollow disc).

Below, the limitations of the crack-sizing algorithm for cracks of nonzero orientation are explored. It must be noted that the error is not symmetrical about the line $x = x_i$. The closer x_i lies to the z-axis, the greater the change in ϕ_i caused by an error in the estimation of x_i and hence the larger the error in the recovered crack size. Assuming x_i is positive, the maximum possible error in the recovered crack length is achieved when the root is estimated at $x_i - p$. And so, from (17), see (21) next page. By Taylor expanding, an analytical approximation for the maximum error ε^{A} is obtained as in (22), see next page. It can be seen from (22) that allowing the pitch $p \to 0$, it follows that $\varepsilon^{\mathrm{A}} \to 0$. This is reiterated in Figs. 4 and 5, which demonstrate the effect of an increasing array pitch on the maximum relative error, $\hat{\varepsilon}^{\mathrm{M}} = \varepsilon^{\mathrm{M}}/a$ (dotted), the analytical approximation of the maximum relative error, $\hat{\varepsilon}^{\mathrm{A}}$

$$\begin{aligned}\hat{a}^{\mathrm{M}} &= \frac{\sqrt{M^2((x_i-p)^2+r^2)-16\pi^2\hat{a}_2^2(r\cos\theta-(x_i-p)\sin\theta)^2}}{2\pi((x_i-p)\cos\theta+r\sin\theta)} \\ &= \left(M^2(x_i^2+r^2)-16\pi^2\hat{a}_2^2(r\cos\theta-x_i\sin\theta)^2+M^2(p^2-2x_ip)-16\pi^2\hat{a}_2^2p\sin\theta(p\sin\theta-2x_i\sin\theta+2r\cos\theta)\right)^{1/2} \\ &\quad\times\left(2\pi(x_i\cos\theta+r\sin\theta)-2\pi p\cos\theta\right)^{-1}.\end{aligned} \tag{21}$$

$$\varepsilon^{\mathrm{A}} = \left|\frac{M^2(p^2-2x_ip)-16\pi^2\hat{a}_2^2p\sin\theta(p\sin\theta-2x_i\sin\theta+2r\cos\theta)}{8\pi^2\hat{a}(x_i\cos\theta+r\sin\theta)^2}+\frac{\hat{a}p\cos\theta}{x_i\cos\theta+r\sin\theta}\right|. \tag{22}$$

$= \varepsilon^{\mathrm{A}}/a$ (dashed), and the actual relative error incurred $\hat{\varepsilon}^{\mathrm{D}} = \varepsilon^{\mathrm{D}}/a$ (full line; here the known value of θ has been used to isolate the effects of the discretization due to the array element pitch on the error). It can be seen that both the maximum relative error, $\hat{\varepsilon}^{\mathrm{M}}$, and its analytical approximation, $\hat{\varepsilon}^{\mathrm{A}}$, are much bigger than the obtained numerical error. This is because they are calculated from the worst case scenario where the estimated x_i is out by a full pitch p. Although possible, it is more likely that the error in x_i is within $p/2$ of the exact location. The analytical form of the error given by equation (22) has been recalculated for the case where the location of the root is estimated as $x_i - p/2$. This is plotted as a thick full line in Figs. 4 and 5, and although not a strict upper bound on the potential error caused by array discretization, it proves to be a more accurate estimation of the actual errors incurred.

Having examined the effect of discretization via the array pitch on the accuracy of the algorithm, the effect of an error in the estimated orientation of the crack will now be studied. Using values varying by up to 10° from the known value of θ, and inputting the exact value for ϕ_i (to discount the effects of discretization), (14) was calculated. Figs. 6(a) and 6(b) plot the relative error in a against the error ε in the estimated crack orientation $\theta^{\varepsilon} = \theta + \varepsilon$, for a 5-mm crack of orientations 0° and 30°, respectively. From these plots, it can be observed that for the crack size to remain within a 5% error interval, $\varepsilon \leq 2.5°$.

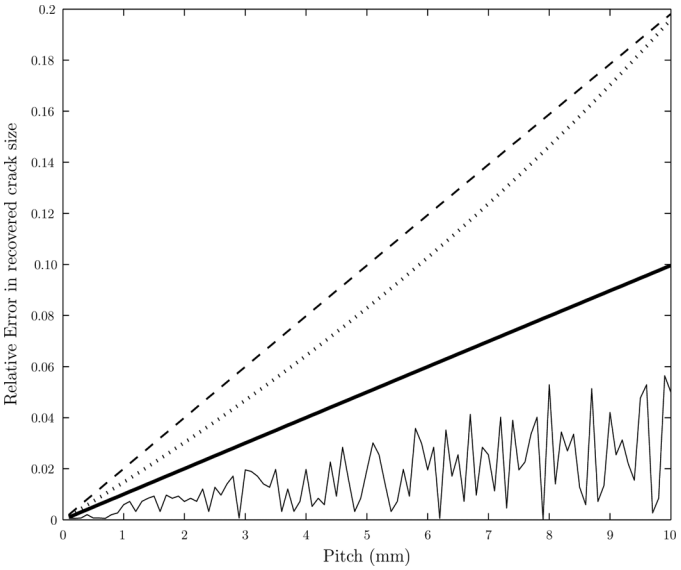

Fig. 4. Relative error in the recovered crack size versus the pitch p for the multi-orientation crack sizing algorithm for a crack with $\hat{a} = 1$ and 0° orientation. Eq. (21) provides $\hat{\varepsilon}^{\mathrm{M}} = \varepsilon^{\mathrm{M}}/a$ (dotted) and equation gives (22) $\hat{\varepsilon}^{\mathrm{A}} = \varepsilon^{\mathrm{A}}/a$ (dashed). $\hat{\varepsilon}^{\mathrm{D}} = \varepsilon^{\mathrm{D}}/a$ (thin full line) plots the actual error obtained using the multi-orientation crack sizing algorithm with the estimated value of x_i taken from the discrete set of points dictated by the array element locations. The thick full line is obtained by substituting $p/2$ for p in (21).

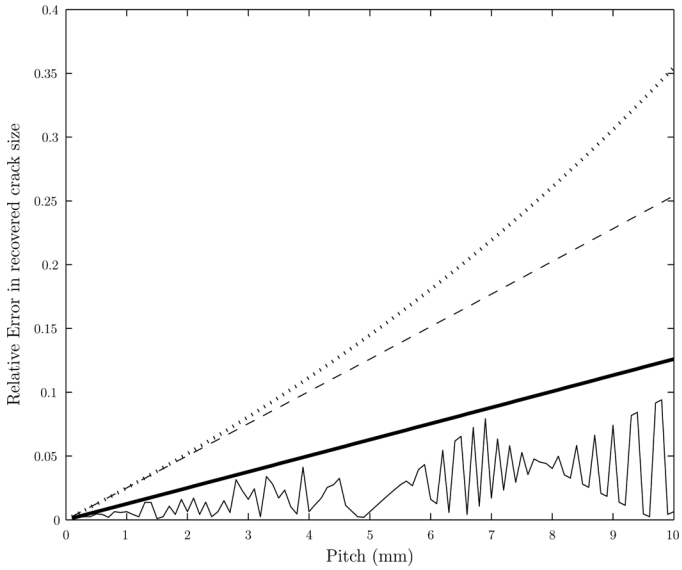

Fig. 5. Relative error in the recovered crack size versus the pitch p for the multi-orientation crack sizing algorithm for a crack with $\hat{a} = 1$ and 30° orientation. Eq. (21) provides $\hat{\varepsilon}^{\mathrm{M}} = \varepsilon^{\mathrm{M}}/a$ (dotted) and (22) gives $\hat{\varepsilon}^{\mathrm{A}} = \varepsilon^{\mathrm{A}}/a$ (dashed). $\hat{\varepsilon}^{\mathrm{D}} = \varepsilon^{\mathrm{D}}/a$ (thin full line) plots the actual error obtained using the multi-orientation crack sizing algorithm with the estimated values of x_i and x_j taken from the discrete set of points dictated by the array element locations. The thick full line is obtained by substituting $p/2$ for p in (21).

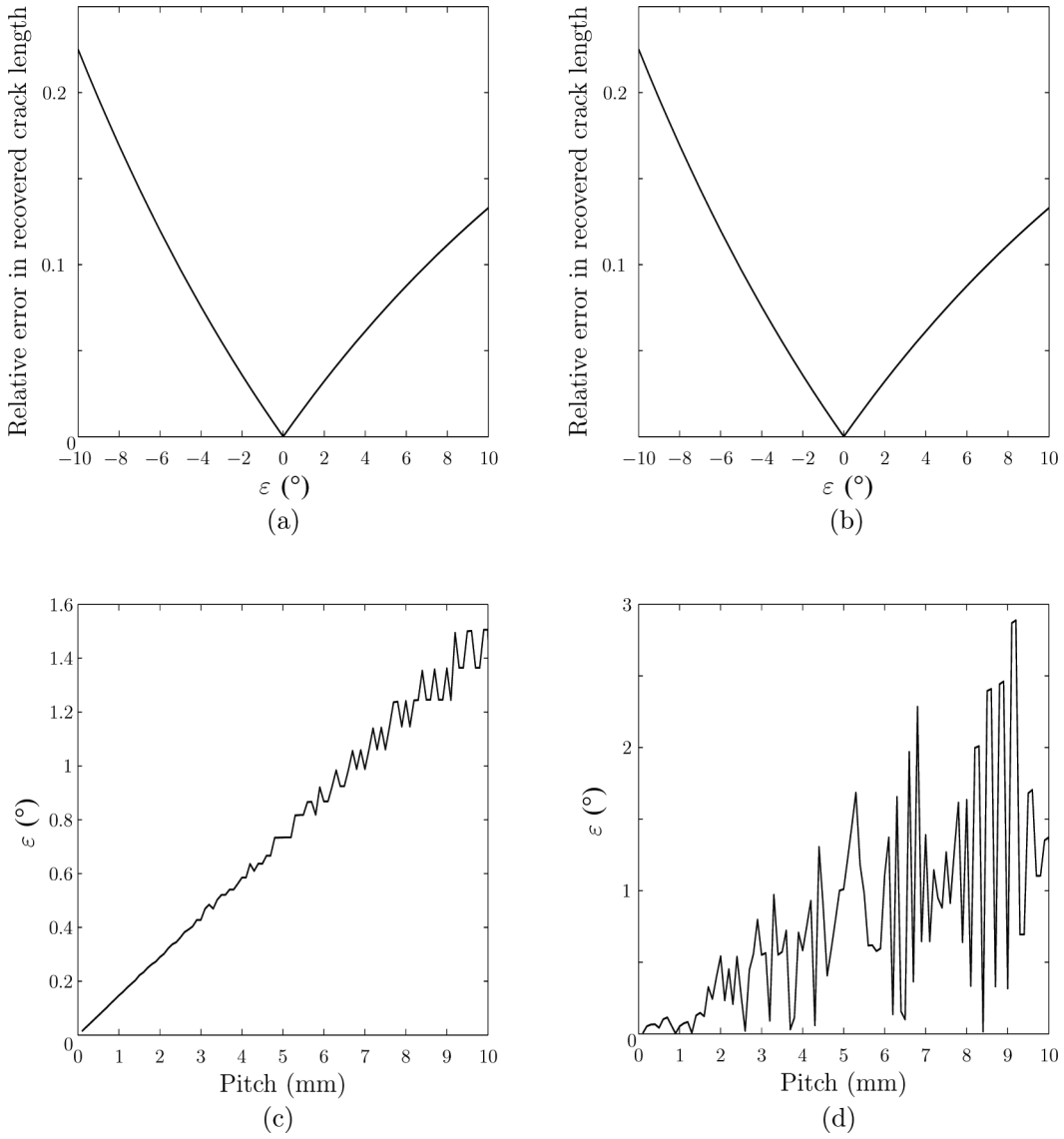

Fig. 6. By inserting the exact angle ϕ_i (the location of the zeros in the pulse-echo response) as calculated in (18) into the crack sizing formula, (14), and keeping all other parameters constant, it is possible to vary θ and analyze the effect that this has on the estimate for the crack size a. The results for cracks oriented at 0° and 30° are plotted in (a) and (b). Plots (c) and (d) track the absolute error in the estimation of θ, calculated via (15), as the pitch increases for cracks oriented at 0° and 30°, respectively. All of the plots shown are plotted for the case where $\hat{a} = 1$.

It can also be noted that Figs. 6(a) and 6(b) are identical, demonstrating that the error in the recovered crack length caused by an error in the estimated orientation is independent of the actual orientation. This becomes obvious by substituting θ^{ε} and (18) into (14); the term $\sin(\phi_i + \theta^{\varepsilon})$ becomes

$$\sin(\sin^{-1}(\sqrt{(M^2\lambda^2 - 16\pi^2 a_2^2)/16\pi^2(a_1^2 - a_2^2)}) + \varepsilon)$$

and is independent of θ [this is similarly true for $\cos(\phi_i + \theta^{\varepsilon})$].

Figs. 6(c) and 6(d) show the absolute error in θ calculated via (15) as the pitch p increases (with set array length of 500 mm and a flaw embedded at a depth of 50 mm from the array, where $\hat{a} = 1$). It can be observed in Fig. 6(c) that even in the extreme case where the pitch is 10 mm, the error in the estimated orientation for the case where $\theta = 0°$ is only 1.6°, well below the upper bound of 2.5°. In the case where $\theta = 30°$ [Fig. 6(d)], the pitch can be increased to approximately 9 mm while remaining within the 2.5° interval. In both cases, (15) provides a suitable estimate of θ over the range of array pitches usually used within the NDT industry (0.5 to 2 mm) and is hence viable for the purpose of the multi-orientation crack-sizing algorithm derived in this paper.

D. Sensitivity Analysis

To assess the potential for further application of the crack-sizing algorithm described in Section II-B, it is interesting to examine the sensitivity of the algorithm to errors in the system parameters. As successful recovery of the crack size is based primarily on a good estimation of ϕ_i, it is interesting to know how relative errors in the

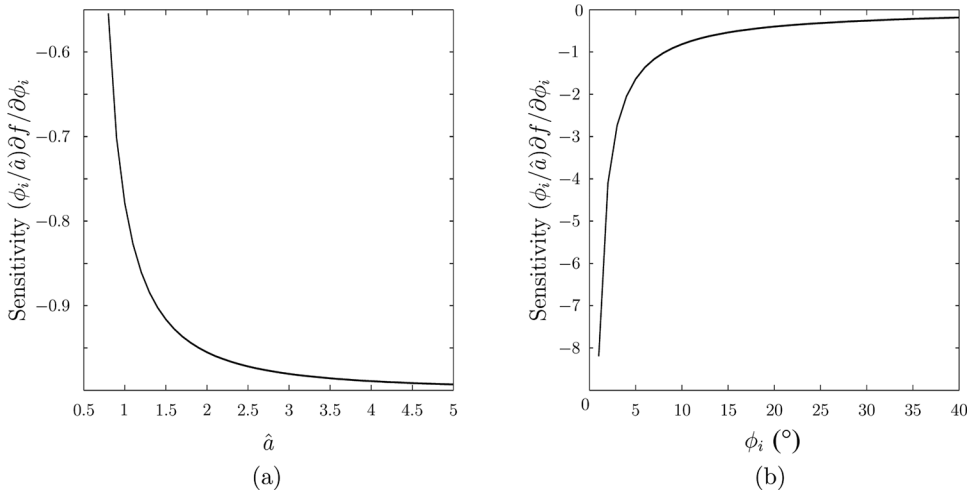

Fig. 7. These plots demonstrate the sensitivity of the algorithm to changes in ϕ_i (the location of the zeros in the pulse-echo response) as (a) $\hat{a}$ increases and (b) ϕ_i increases.

approximation of ϕ_i will affect the recovered crack size estimate. To analyze this, from (14), let

$$\hat{a} = \sqrt{\frac{M^2}{4\pi^2}\csc^2(\phi_i+\theta) - 4\left(\frac{a_2}{\lambda}\right)^2 \cot(\phi_i+\theta)} = f(\phi_i). \tag{23}$$

Then

$$\frac{\partial f}{\partial \phi_i} = \frac{2\cot(\phi_i+\theta)(16\pi^2\hat{a}_2^2 - M^2)}{4\pi\sin(\phi_i+\theta)(M^2 - 16\pi^2\hat{a}_2^2\cos^2(\phi_i+\theta))^{1/2}}. \tag{24}$$

The relative effects of changes in the estimated angle of reception, ϕ_i, on the crack size relative to the wavelength, $\hat{a}$, can be calculated from

$$\frac{\Delta\hat{a}}{\hat{a}} = \frac{\partial f}{\partial\phi_i}\frac{\phi_i}{\hat{a}}\frac{\Delta\phi_i}{\phi_i}. \tag{25}$$

Fig. 7(a) plots $(\phi_i/\hat{a})\partial f/\partial\phi_i$ against $\hat{a} = a/\lambda$, demonstrating the sensitivity of the relative error in $\hat{a}$ due to variations in ϕ_i as $\hat{a}$ increases. For example, the relative error in the recovered crack length to wavelength ratio when $\hat{a} = 1$ will be around 0.85 times the relative error in the estimated parameter ϕ_i (assuming that all other measurements are correct). For the case where $\hat{a} = 2$, the relative error in the recovered crack length to wavelength ratio will be around 0.95 times the relative error in the estimated parameter ϕ_i. And so, it can be observed that as the value of $\hat{a}$ increases, the sensitivity of the crack sizing algorithm to errors in ϕ_i increases. To help explain this, recall that as $\hat{a}$ increases, the width of the scattering matrices central lobe decreases, and hence, the elements at which the zeros of the pulse-echo response plot reside are located closer to the vertical axis. The closer the zero of the pulse-echo response to the vertical axis, the greater the change in ϕ_i between neighboring array elements, and hence, the larger the potential error in the recovered crack size. This is corroborated in Fig. 7(b) where it is shown that as ϕ_i increases, the sensitivity of the crack-sizing algorithm to changes in ϕ_i decreases.

III. Application to Experimental Data

The test sample considered in this paper is manufactured from 316L stainless steel and constructed from welded austenitic plates with implanted defects. The defect of interest is a 6 mm lack-of-fusion crack between the weld and plate, lying at a 50° angle with respect to the x-axis (see Fig. 8). The inspection was carried out by the 5-MHz linear array (Vermon, Tours, France) as specified in Table I combined with the Dynaray (Zetec, Quebec, QC, Canada) array controller. A full matrix capture was collected from the sample where the array was positioned as depicted by the shaded region in Fig. 8. TFM images were constructed (with an experimentally derived pressure wave speed of 5820 m/s) to validate the location of the defect, allowing scattering matrices to be generated over the relevant time windows.

A. Model-Based Optimization

So far in this paper, it has been demonstrated how a mathematical model can be used to derive formulae for the characterization of zero-volume flaws, given a frequency domain scattering matrix. This analytical formulation allows for insight into the effects of individual parameters on the ability of the algorithm to correctly size a defect.

TABLE I. Transducer Specifications.

Ultrasonic transducer array parameter	Value	Unit
Number of array elements	128	—
Pitch	0.7	mm
Transducer center frequency	5	MHz
Bandwidth (−6 dB)	60	%

However, the method is reliant on the approximation of the roots (or local minima) of the pulse-echo response. This is fine when the data arise from a flaw embedded in a perfectly homogeneous host material, but if the material is heterogeneous then a different tactic is required. The full line in Fig. 9 demonstrates the difficulty in extracting the location of these roots from pulse-echo responses arising from experimentally collected data (see Section III) as multiple minima and multiple peaks can be observed. Another complication in applying the formulae to experimental data is that the formulae have been developed for the scenario where the crack is located directly underneath the center of the array. This is rarely the case in practice. As a move of the flaw from the origin causes a shift in the location of the maximum peak in the scattering matrix, it becomes difficult to extract a reasonable estimate of crack orientation and thus the formulae become unreliable. This is demonstrated in Fig. 9. The dashed line represents the pulse-echo response as generated by the Born approximation for a crack of 40° relative to the x-axis. This lies neatly on the full line which has been generated by the experimental FMC data. However, the crack within the experiment lies at an angle of 50° with respect to the x-axis and should lie underneath the dotted line, which is the model for a crack at this orientation. Thus it is not possible to implement the model-based crack-sizing algorithm in its current form to these cases. Instead, the model will now be used as a basis for an optimization technique, which will importantly retain the objective nature of the final crack size estimate. This optimization technique utilizes the full scattering matrix, in contrast to the pulse-echo-based methods explored above, and hence exploits more of the data available to us through phased array inspections.

To implement the method, the elements of the model scattering matrix F^{B} are calculated by the Born approximation,

$$F^{B}_{i,j}(a,f) = \frac{a a_2 B_{ln} f_l(\mathbf{e}_i,\mathbf{e}_j)}{2|\mathbf{g}|^2 (r_{\mathrm{e}})^2} \times \left(\frac{\sin(k_0|\mathbf{g}|r_{\mathrm{e}}) - k_0|\mathbf{g}|r_{\mathrm{e}}\cos(k_0|\mathbf{g}|r_{\mathrm{e}})}{k_0|\mathbf{g}|r_{\mathrm{e}}} \right), \tag{26}$$

where a_2, k_0, r_{e}, $\mathbf{g}$, and $B_{ln}f_l(\mathbf{e}_i,\mathbf{e}_j)$ are as defined in Section I-A. The vectors $\mathbf{e}_i$ and $\mathbf{e}_j$ are chosen as the transmit and receive directions (respectively) arising from the location and dimensions of the array used in the experiment. Having fixed all these parameters, the scattering matrix F^B is solely dependent on the crack length a and frequency f. For each crack length and frequency pair, the elements of F^B are summed and then subtracted from the sum of the elements of the experimental scattering matrix at the corresponding frequency,

$$S_{a,f} = || \sum_{i}^{N}\sum_{j}^{N} F^{B}_{i,j}(a,f) - \sum_{i}^{N}\sum_{j}^{N} F^{e}_{i,j}(f) \, || \, . \tag{27}$$

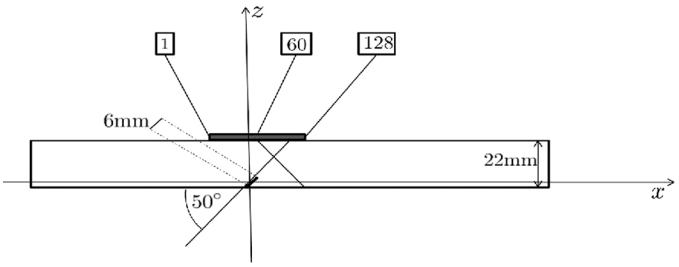

Fig. 8. The schematic depicts a cross-section (the x-z plane) of the stainless steel test sample constructed from welded austenitic plates of 22 mm depth. A lack-of-fusion crack of 6 mm height lies along the left-hand side of the weld at an angle of 50° with respect to the x-axis. The location of the array is marked by the shaded gray box and the labels 1, 60, and 128 mark the location of key elements which lie at (−37.1 mm, 16 mm), (4.2 mm, 16 mm), and (51.8 mm, 16 mm) with respect to the flaw, which is situated at the origin.

This is carried out over some range of crack lengths $l \leq a \leq m$ and some range of frequencies $q \leq f \leq r$, where q and r are dictated by the bandwidth of the transducer employed in the experiment. Using the known minimum frequency of the transducer bandwidth, the longest wavelength λ_l can be calculated and the lower bound on crack length chosen as $l = M\lambda_l/2\pi$ [so that (9) holds]. The upper bound m is chosen to be 50% of the total depth of the sample (it is assumed cracks larger than this are easily characterized using conventional imaging techniques). The matrix S will be referred to as the objective sizing matrix (OSM). Note that the scattering amplitudes have been normalized by dividing each element by the value of the largest element, and thus the optimization is dependent only on the shape of the scattering profile. It is anticipated

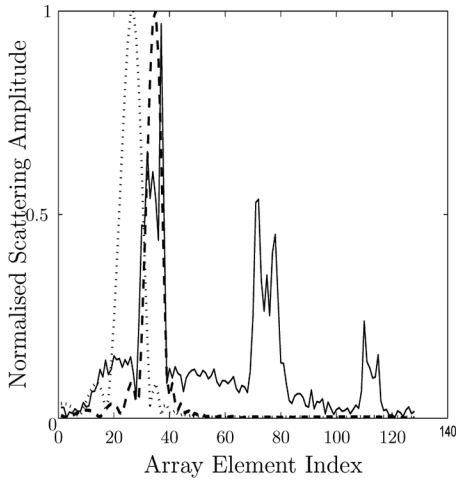

Fig. 9. This plot depicts the pulse-echo response taken from experimentally collected data arising from a lack-of-fusion crack of 6 mm length and 50° orientation (relative to the x-axis) lying between a stainless steel weld and plate. The data arise from inspection by a 128-element linear array and are examined here at the center frequency of 5 MHz (full line). The comparable pulse-echo responses as generated by the Born approximation using the same system parameters for cracks of 40° and 50° orientation (relative to the x-axis) are plotted by the dashed and dotted lines, respectively.

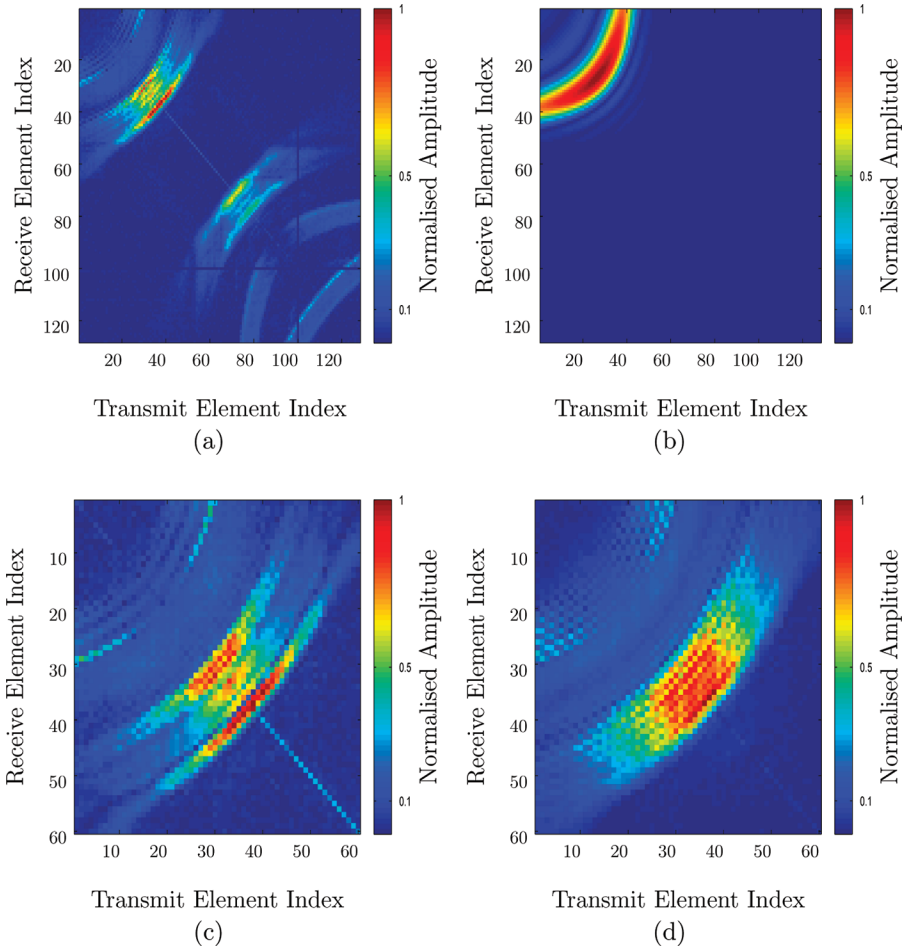

Fig. 10. Plot (a) depicts the scattering matrix as generated from experimental FMC data over the full 128 elements. Plot (b) has been generated by the Born approximation, mimicking the parameters of the experimental set up. Plot (c) is obtained from a subset of the experimental data (the signals collected by the first 60 elements of the array) as described in Section III and is plotted at a frequency of 3.5 MHz. Plot (d) arises from the same data but is plotted at a frequency of 6.5 MHz.

that the global minimum of the OSM will relate to the actual crack length.

B. Scattering Submatrices

To apply the model-based optimization crack-sizing method to experimental data, it is prudent to first minimize the gap between the model and experiment. It must be recalled that the Born approximation is concerned only with predicting the scattering by an ellipsoidal flaw; transduction effects, material heterogeneities, material attenuation, diffraction, refraction, and reflections from experimental artifacts other than the flaw are not considered. Additionally, the experimental data undergo discretization in the transformation from the time domain to the frequency domain via the FFT and so do not exhibit the continuous spectrum of frequencies available to the model. Thus an exact match between scattering matrices arising from the model and experiment is not anticipated. However, steps can be taken to increase the consonance between the two. This can be achieved by isolating the scattering pertaining to the crack from the scattering by other features (e.g., the front face, the back wall, and heterogeneities) where possible. To do this, it is assumed that the location of the flaw is known and a discrete Fourier transform is applied to the relevant time window. Due to the close proximity of the crack to the back wall in the sample as described in Section III, it is expected that in the chosen time interval, the received signals (particularly those arising from elements lying further from the crack) will include high amplitudes from scattering by the backwall. This can be seen in Fig. 10(a), where the scattering matrix arising from the experiment is plotted at the central operating frequency of 5 MHz. Fig. 10(b) has been generated by the Born approximation, mimicking the experimental setup that gave rise to Fig. 10(a). It can be observed that a secondary lobe emerges in the lower right segment of the matrix in Fig. 10(a) where there is none in Fig. 10(b). This can be attributed to interference by the back wall. To combat this, the scattering matrix can be cropped by using only signals collected by the first 60 elements of the array, which importantly incorporate the signals closest to the specular reflection by the crack. It is assumed that the scattering by the crack which is ignored by the exclusion of elements is negligible as a longer travel time is involved and the scattering is therefore sub-

ject to more attenuation. Fig. 10(c) and (d) depict such submatrices (arising from the experimental FMC data). These scattering submatrices are plotted at 3.5 and 6.5 MHz, respectively (the outer limits of the transducer's bandwidth). The high-amplitude pulse-echo response (the diagonal of the scattering matrix) observed in Fig. 10(c) can be attributed to the ring down of the array elements, where the transmitted wave from the transmitting element can initially interfere with the reception of that same element. This effect is overshadowed when the scattering amplitude is large as in Fig. 10(d).

Now that the secondary peaks of the scattering matrix have been effectively removed, it is interesting to know whether the remaining peak bears any resemblance to those predicted by the Born approximation. The pulse-echo response as shown in Fig. 9 is used as a test case. It can be seen already that the width of the tallest lobe seems to correlate reasonably with that modeled by the Born approximation. Using the formulae given in (18), and allowing the flaw orientation to be 40° so that the model pulse-echo response aligns with that of the experiment, the roots of the pulse-echo response are estimated to occur at −18 and −10 mm along the array. Given that the array begins at −37.1 mm (so that the flaw lies on the origin, see Fig. 8) and the pitch is 0.7 mm, this translates to element indices 27 and 39, which closely correspond to the innermost minima of the experimental pulse-echo response shown in Fig. 9 at indices 28 and 39 (although a discrepancy between the two estimations of the left-hand roots is apparent, the pitch is small so the error is small too, see Figs. 4 and 5). Hence there exists some correspondence between the width of the central lobe of the scattering matrix as generated by the experiment and the model, despite the differences listed in Section III-B. Furthermore, it can be noted that these elements lie within the scattering submatrices shown above and hence the formulae could potentially be used to guide the cropping process in the case where heterogeneities obscure the lobes of the scattering matrix.

C. Experimental Results

The results shown in Fig. 11 have been generated by application of the optimization technique to submatrices of size 60 × 60 (as discussed in Section III-B), arising from the data generated by the experiment detailed in Section III. As the crack is not located centrally under the array, the location of the maximum amplitude of the pulse-echo response of the scattering matrix (where $e_i = -e_j$) is no longer a reliable indication of the crack orientation. However, it can still be used to tailor the model-based scattering matrices to those arising from the experiment. By taking the location of the maximum of the pulse-echo response of the experimental scattering matrix at each frequency lying within the interval determined by the bandwidth of the transducer (3.5 to 6.5 MHz) and comparing it to that of scattering matrices generated by the Born approximation, an orientation can be extracted.

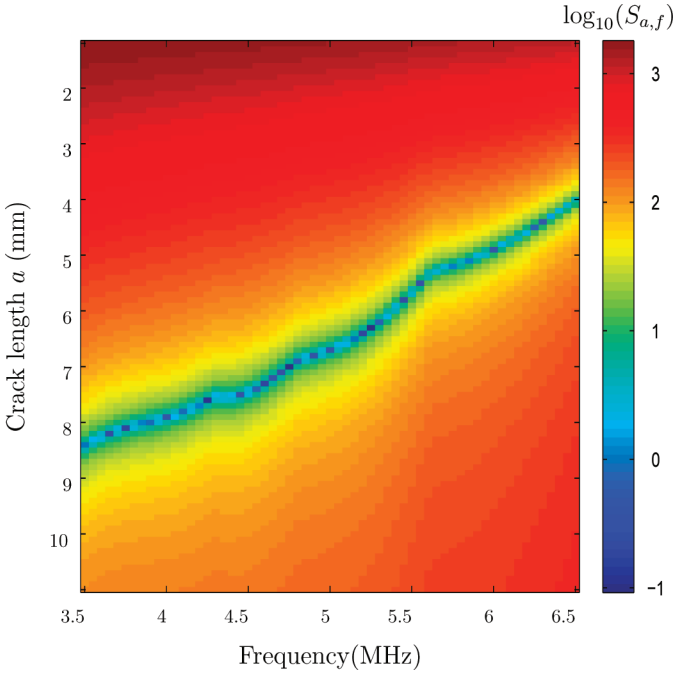

Fig. 11. Plot of the objective sizing matrix for the data set arising from the experiment as described in Section III, computed over the range of frequencies determined by the bandwidth of the transducer (3.5 to 6.5 MHz).

Averaging over these frequencies, an objective estimate of 39.7° (with respect to the x-axis) was reached, giving way to an absolute error of 10.3°. Fig. 11 displays the objective sizing matrix (plotted on a logarithmic scale to allow closer inspection of the minima) calculated by exploiting the 60 × 60 elements of the scattering submatrix taken over the bandwidth of the transducer. As the lowest frequency of the transducer's bandwidth gives rise to a wavelength of $\lambda_l = 1.7$ mm, it follows that the range of crack sizes considered should be greater than $M\lambda_l/2\pi = 1.2$ mm. The maximum crack length was chosen here as 11 mm, half the depth of the sample. The cost function as given by (27) is calculated for every crack length and frequency pair where the Born approximation assumes the crack orientation to be the already estimated 39.7°. Recall that the shape of the scattering matrix is dependent on a/λ. As the experimental scattering matrices are plotted for a constant (unknown) crack length over a range of increasing frequencies, the a/λ value increases systematically. In comparing the scattering matrices arising from the experiment to those as generated by the model over a range of crack lengths and frequencies, it is this a/λ value that dictates where the minima occur, thus explaining the positive linear trend of the minima. From Fig. 11, it can be observed that the global minimum occurs when the crack length is equal to 7 mm at a frequency of 4.75 MHz. However, there exist multiple local minima lying along the blue line of Fig. 11 and their respective amplitudes are quite similar. Therefore the position of the global minimum is sensitive to noise arising from experimental artifacts (e.g., scattering by the back wall or heterogeneities).

To combat this and increase the robustness of the algorithm, a multi-frequency averaging approach is adopted; for simplicity a uniform average is taken rather than some frequency weighted approach. Taking the global minimum of each column of the OSM and averaging, the objective crack length estimation of 6.4 mm is obtained (recall the actual crack length is 6 mm).

IV. Conclusions

A model-based approach to crack-sizing via the Born approximation has been derived. Through the analysis of the pulse-echo diagonal of the scattering matrices, it was observed that the distance between the zeros surrounding the central lobe correlated with the crack length. Using these zeros, a formula was derived to extract the crack length from the scattering matrices for the case where a single crack lay parallel (zero degrees orientation) to an ultrasonic, linear array. This was then extended to cover cracks of nonzero orientation. Subsequently, it was discovered that the orientation could also be extracted from knowledge of the placement of the two innermost roots in the pulse-echo response plot. An analytical expression for the maximum error caused by discretization arising from the finite extent of the array pitch p was derived for both cases. It was shown that as the array pitch p tended to zero, this error also tended to zero. The error in the approximation of the crack orientation, θ, was also studied and it was shown that the resulting error in recovered crack size was independent of the actual crack orientation. Through a sensitivity analysis, it was observed that the algorithm was susceptible to errors in the measurement of the zeros in the pulse-echo profile. Thus, obtaining an accurate value for these roots is key to the method's success. As shown in the error analysis, this can be achieved by using as small an array element pitch as possible.

Although the crack sizing algorithm proved interesting from a mathematical perspective, providing analytical insight into the effects of array pitch and length, crack length to wavelength ratio, frequency and flaw depth, it was deemed unsuitable for application to experimentally collected data from heterogeneous materials, due to the difficulty of extracting the zeros (or local minima) of the pulse-echo response curve and the limiting condition that the crack must lie under the center of the array. Hence, it was decided to use the model as a basis for an optimization technique, which importantly retained the objectivity of the final crack length estimate. The scattering matrices arising from the collected experimental data were compared with those constructed by the Born approximation over a range of frequencies and crack lengths. First, the global minimum was taken as the objective crack length measurement; however, a multi-frequency averaging approach was soon adopted to increase the algorithm's robustness to noise. In application to the available experimental data, this approach provided an objective crack length estimate of 6.4 mm for an actual crack of length 6 mm.

V. Data Accessibility

This work was supported by the Engineering and Physical Sciences Research Council (grant number EP/I019731/1). The research data associated with this paper will become available at the following link: http://dx.doi.org/10.15129/a7da5071-0436-4913-8f0e-de78f5ebccd6.

Acknowledgments

This work was funded through the UK Research Centre in NDE Targeted Programme by the Engineering and Physical Sciences Research Council (grant number EP/IO19731/1), National Nuclear Laboratory, Rolls Royce, Shell, Weidlinger, and Amec Foster Wheeler, who also provided the experimental sample. The authors thank T. Lardner for collecting the FMC data.

References

[1] M. Cherfaoui, "Innovative techniques in non-destructive testing and industrial applications on pressure equipment," *Procedia Eng.*, vol. 46, pp. 266–278, 2012.

[2] H. W. Liu, S. P. Zhan, Y. H. Du, and P. Zhang, "Study on pulsed eddy current nondestructive testing technology for pipeline corrosion defects based on finite element method," *Applied Mech. Mater.*, vol. 120, pp. 36–41, 2012.

[3] U. Schnars and R. Henrich, "Applications of NDT methods on composite structures in aerospace industry," in *Conf. on Damage in Composite Materials, Stuttgart, Germany*, 2013, pp. 1–8.

[4] C. Holmes, B. W. Drinkwater, and P. D. Wilcox, "Post-processing of the full matrix of ultrasonic transmit receive array data for non destructive evaluation," *NDT Int.*, vol. 38, no. 8, pp. 701–711, 2005.

[5] B. W. Drinkwater and P. D. Wilcox, "Ultrasonic arrays for non-destructive evaluation: A review," *NDT Int.*, vol. 39, no. 7, pp. 525–541, 2006.

[6] J. Davies, F. Simonetti, M. Lowe, and P. Cawley, "Review of synthetically focused guided wave imaging techniques with application to defect sizing," *AIP Conf. Proc.*, vol. 820, no. 142, pp. 142–149, 2006.

[7] J. Camacho, M. Parrilla, and C. Fritsch, "Phase coherence imaging," *IEEE Trans. Ultrason. Ferroelectr. Freq. Control*, vol. 56, no. 5, pp. 958–974, 2009.

[8] J. Zhang, B. W. Drinkwater, and P. D. Wilcox, "Comparison of ultrasonic array imaging algorithms for nondestructive evaluation," *IEEE Trans. Ultrason. Ferroelectr. Freq. Control*, vol. 60, no. 8, pp. 1732–1745, 2013.

[9] L. Borcea, G. Papanicolaou, and C. Tsogka, "Coherent interferometric imaging in clutter," *Geophysics*, vol. 71, no. 4, pp. 165–175, 2006.

[10] J. Zhang, B. W. Drinkwater, and P. D. Wilcox, "The use of ultrasonic arrays to characterize crack-like defects," *J. Nondestruct. Eval.*, vol. 29, no. 4, pp. 222–232, 2010.

[11] P. M. Morse and K. U. Ingard, *Theoretical Acoustics*, Princeton, NJ, USA: Princeton University Press, 1968.

[12] L. W. Schmerr, *Fundamentals of Ultrasonic Nondestructive Evaluation: A Modelling Approach*, New York, NY, USA: Plenum Press, 1998.

[13] J. L. Rose, *Ultrasonic Waves in Solid Media*, Cambridge, UK: Cambridge University Press, 1999.

[14] H. Sato and M. Fehler, *Seismic Wave Propagation and Scattering in the Heterogeneous Earth*, Berlin, Germany: Springer-Verlag, 2012.

[15] J. Zhang, B. W. Drinkwater, and P. D. Wilcox, "Defect characterization using an ultrasonic array to measure the scattering coefficient matrix," *IEEE Trans. Ultrason. Ferroelectr. Freq. Control*, vol. 55, no. 10, pp. 2254–2265, 2008.

[16] J. W. Hunt, M. Arditi, and F. S. Foster, "Ultrasound transducers for pulse-echo medical imaging," *IEEE Trans. Biomed. Eng.*, vol. 30, no. 8, pp. 453–481, 1983.
[17] J. A. Jensen and N. B. Svensden, "Calculation of pressure fields from arbitrarily shaped, apodized, and excited ultrasound transducers," *IEEE Trans. Ultrason. Ferroelectr. Freq. Control*, vol. 39, no. 2, pp. 262–267, 1992.
[18] J. H. Rose, "Elastic wave inverse scattering in nondestructive evaluation," *Scattering and Attenuation of Seismic Waves, Part II*, New York, NY, USA: Springer, 1989, pp. 715–739.

Katherine Tant was born in Edinburgh, Scotland, in 1988. She received her B.Sc. Honours degree in mathematics from Heriot-Watt University in 2011 and her Ph.D. degree from the University of Strathclyde in 2014. Her Ph.D. thesis was on the mathematical modelling of scattered waves for application in NDT. She currently works as a research associate within the Department of Mathematics and Statistics at the University of Strathclyde, collaborating closely with academics in the Centre of Ultrasonic Engineering at Strathclyde. Her research interests include scattering theory, inverse problems, and ultrasonic NDT.

Tony Mulholland was born in Glasgow, Scotland, UK, in 1966. He received a B.Sc. Honours degree in mathematics from the University of Glasgow in 1987, an M.Sc. degree in industrial mathematics from the University of Strathclyde in 1991, and a Ph.D. degree in mathematical biology from Glasgow Caledonian University in 1994. From 1999 he has been an academic member of staff in the Department of Mathematics and Statistics at the University of Strathclyde, where he is now a Reader. He has worked with the Centre for Ultrasonic Engineering (CUE) at the University of Strathclyde since 1996 and he now leads the modelling activities of the centre. He has published over 70 papers in applied mathematics, particularly in the modelling of ultrasonic devices and systems. He has been funded by EPSRC on several grants (EP/K028049/1, EP/K014250/1, EP/I019731, EP/F017421, EP/E018858, GR/S31235, GR/N27644, GR/N02207, EP/L022125/1), and by industry partners such as the National Nuclear Laboratory, Rolls-Royce, Serco Assurance (Risley), Shell, Weidlinger Associates, BP, GSK, Astra Zeneca, and Doosan Power Systems. He has undertaken various leadership roles within the academic community and he has been the Vice Dean for Knowledge Exchange in the Faculty of Science at Strathclyde since 2010.

Anthony Gachagan is the Director of the Centre for Ultrasonic Engineering (CUE), based in the Department of Electrical and Electronic Engineering (EEE) at Strathclyde University. He received his Ph.D. degree from the University of Strathclyde in 1996 for the development of air-coupled piezoelectric transducer technology. He has worked in the field of ultrasound for over 20 years and is the author of over 100 research publications across a broad application range including non-destructive evaluation (NDE), sonar, bioacoustics, and industrial process control. His specific research interests encompass ultrasonic transducers and arrays, array imaging processing, power ultrasound, industrial process control instrumentation, and the application of coded excitation techniques.